Machine learning-based pulse wave analysis for classification of circle of Willis topology: An in silico study with 30,618 virtual subjects

Ahmet Sen, Miquel Aguirre, Peter H Charlton, Laurent Navarro, Stéphane Avril, Jordi Alastruey

Biomedical Signal Processing and Control 100 (2025) 106999

Contents lists available at ScienceDirect

Biomedical Signal Processing and Control

journal homepage: www.elsevier.com/locate/bspc

Machine learning-based pulse wave analysis for classification of circle of Willis topology: An *in silico* study with 30,618 virtual subjects

Ahmet Sen [a,e], Miquel Aguirre [a,b,c], Peter H Charlton [d], Laurent Navarro [a], Stéphane Avril [a], Jordi Alastruey [e,*]

[a] Mines Saint-Etienne, Univ Jean Monnet, Etablissement Français du Sang, INSERM, U 1059 Sainbiose, F-42023, Saint-Etienne, France
[b] Laboratori de Càlcul Numèric, Universitat Politècnica de Catalunya, Jordi Girona 1, E-08034 Barcelona, Spain
[c] International Centre for Numerical Methods in Engineering (CIMNE), Gran Capità, 08034 Barcelona, Spain
[d] Department of Public Health and Primary Care, University of Cambridge, Cambridge, UK
[e] Department of Biomedical Engineering, School of Biomedical Engineering and Imaging Sciences, King's College London, London, UK

ARTICLE INFO

Keywords:
Circle of Willis
Anatomical variations
Haemodynamics
Machine Learning
Pulse wave

ABSTRACT

Background and Objective: The topology of the circle of Willis (CoW) is crucial in cerebral circulation and significantly impacts patient management. Incomplete CoW structures increase stroke risk and post-stroke damage. Current detection methods using computed tomography and magnetic resonance scans are often invasive, time-consuming, and costly. This study investigated the use of machine learning (ML) to classify CoW topology through arterial blood flow velocity pulse waves (PWs), which can be noninvasively measured with Doppler ultrasound.

Methods: A database of *in silico* PWs from 30,618 virtual subjects, aged 25 to 75 years, with complete and incomplete CoW topologies was created and validated against *in vivo* data. Seven ML architectures were trained and tested using 45 combinations of carotid, vertebral and brachial artery PWs, with varying levels of artificial noise to mimic real-world measurement errors. SHapley Additive exPlanations (SHAP) were used to interpret the predictions made by the artificial neural network (ANN) models.

Results: A convolutional neural network achieved the highest accuracy (98%) for CoW topology classification using a combination of one vertebral and one common carotid velocity PW without noise. Under a 20% noise-to-signal ratio, a multi-layer perceptron model had the highest prediction rate (79%). All ML models performed best for topologies lacking posterior communication arteries. Mean and peak systolic velocities were identified as key features influencing ANN predictions.

Conclusions: ML-based PW analysis shows significant potential for efficient, noninvasive CoW topology detection via Doppler ultrasound. The dataset, post-processing tools, and ML code, are freely available to support further research.

1. Introduction

The brain is crucially dependent on the cerebral circulation due to its high metabolic rate and sensitivity to ischemia. Vascular structures such as the circle of Willis (CoW) and flow autoregulation ensure adequate blood supply to the brain. The CoW is a ring-like arterial structure located at the base of the brain that supplies the anterior cerebral arteries (ACAs) and middle cerebral arteries (MCAs) – which perfuse the anterior cerebral circulation – and the posterior cerebral arteries (PCAs) – which perfuse the posterior circulation (Fig. 1B). Both circulations are interconnected by the anterior and posterior communicating arteries (ACoA and PCoAs, respectively). The CoW provides collateral blood flow to the efferent (outflow) arteries (i.e., ACA, MCA, and PCA) if cerebral arteries are missing or if afferent (inflow) arteries (i.e., carotid, vertebral, and basilar arteries) are obstructed [3,4]. About half of the population has an incomplete CoW, where at least one artery is missing [32,19], increasing stroke risk and post-stroke permanent damage in subjects with severe stenosis in the afferent arteries [18,17]. An incomplete CoW is also associated with atherosclerosis plaque development [29], post-surgery intracerebral haemorrhage [55], intracranial

* Corresponding author at: Department of Biomedical Engineering, King's College London, St. Thomas' Hospital, London SE1 7EU, United Kingdom.
E-mail address: jordi.alastruey-arimon@kcl.ac.uk (J. Alastruey).

https://doi.org/10.1016/j.bspc.2024.106999
Received 8 February 2024; Received in revised form 16 September 2024; Accepted 30 September 2024

aneurysms [44], white matter disease [45], and brain ageing [62]. There are over 40 anatomical variations of the CoW [19].

Magnetic resonance angiography (MRA) and computed tomography angiography (CTA) are currently used to identify CoW topology [19,60,52]. However, these methods are costly, time-consuming, and require specialist equipment and trained operators. Additionally, they involve the use of ionising radiation or contrast agents, which carry risks for patients. These issues restrict the practicality of MRA and CTA, especially in lower-resource settings [31,13]. Studies have shown relationships between CoW variations and flow rates in carotid, basilar, and cerebral arteries using MRA and transcranial Doppler ultrasound [51,39], and computational models [see [3] and references therein]. This suggests the possibility of identifying CoW topology by analysing the blood flow wave measured noninvasively using faster and cheaper techniques like Doppler ultrasound. Machine learning (ML) can automate this analysis, potentially identifying complex patterns and associations that are difficult for humans to discern.

ML-based pulse wave (PW) analysis has shown promise in clinical applications such as early cardiovascular disease detection [22,11,21,58], evaluation of blood supply in heart failure patients [57], and early stroke detection [49], offering potentially faster and less invasive approaches compared to traditional methods. Beyond specific applications, ML has the potential to enhance overall diagnostics by identifying subtle changes in pulse waveforms that traditional methods might miss, potentially leading to earlier detection of various cardiovascular diseases [38]. However, training ML models requires large PW databases, and acquiring these data presents challenges, including (i) difficulty in measuring PWs at all relevant locations; (ii) variability in measurement accuracy due to equipment and operator differences; and (iii) the costly and time-consuming nature of data collection. Additionally, evaluating the impact of individual cardiovascular properties on the PW is challenging since other properties may vary due to compensatory effects of cardiovascular homeostatic reflexes. Databases of simulated PWs representative of samples of real subjects offer a complementary approach to *in vivo* datasets, addressing these challenges [12,23,59,61]. These databases can be created for thousands of virtual subjects using computational blood flow modelling over a wide range of cardiovascular conditions, and used for training ML methods [6].

The aim of this study was to investigate the feasibility of ML-based PW analysis for classifying CoW topology using a new database of *in silico* PWs representative of subjects aged 25 to 75 years, with complete and incomplete CoW topologies. The database was created using one-dimensional (1-D) blood flow modelling. Seven ML models were trained, tested, and compared to classify haemodynamic data using different combinations of blood flow velocity PWs obtained in the carotid, vertebral and brachial arteries, with or without the brachial blood pressure PW.

2. Methods

2.1. Dataset of in silico pulse waves

Several PW signals were simulated in the larger systemic arteries (see Fig. 1A), including blood pressure (P), blood flow velocity (U), and blood flow rate (Q) waveforms. The geometrical and material properties of the arterial network and the inflow and outflow boundary conditions of the baseline subjects aged 25, 35, 45, 55, 65, and 75 years with a complete CoW were based on the corresponding baseline subjects from an existing *in silico* PW database [12]. The nonlinear 1-D equations of incompressible and axisymmetric flow in Voigt-type viscoelastic vessels were used to model blood flow. This formulation is based on the physical principles of conservation of mass, momentum, and energy. It assumes laminar flow, incompressible and Newtonian blood properties (density: 1,060 kg/m^3; viscosity: 2.5 mPa·s), parabolic velocity profiles, and no energy losses at bifurcations [6]. (Further details are provided in Supplementary Material Appendix A).

This study focused on the seven most common CoW variations, selected based on population-level frequency and haemodynamic significance of absent cerebral arteries [3,4], as illustrated in Fig. 1B. Each variation was created by removing the missing artery/ies from the

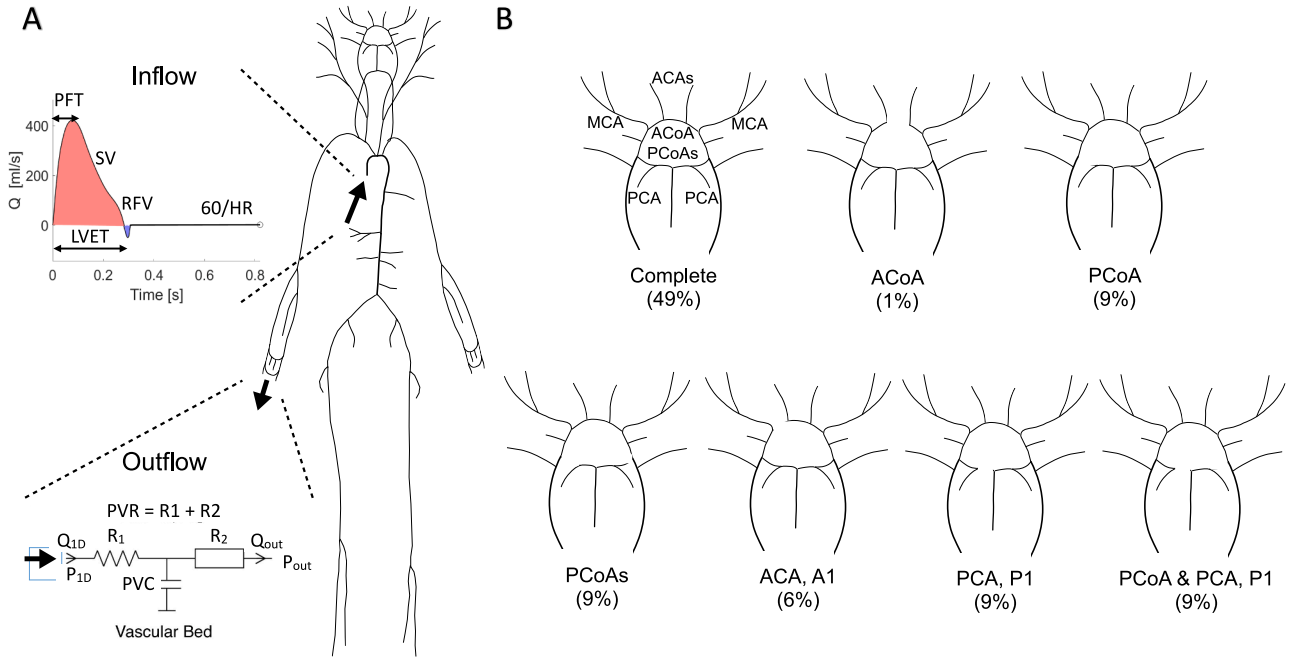

Fig. 1. The one-dimensional (1-D) model of pulse wave propagation (A) and the studied anatomical variations of the circle of Willis (B). The model consists of an arterial network of the larger systemic arteries made up of 1-D model segments, the inflow waveform prescribed at the aortic root, and zero-dimensional (Windkessel) outflow boundary conditions at each terminal segment. The label below each anatomical variation indicates the artery absent and its frequency. ACoA: anterior communication artery; PCoA: either posterior communication artery; PCoAs: both posterior communication arteries; ACA, A1: either anterior cerebral artery A1 level; PCA, P1: either posterior cerebral artery P1 level; PCoA & PCA, P1: posterior cerebral artery P1 level and contralateral posterior communication artery. See Glossary for definition of remaining terms.

Table 1
The modified input cardiovascular parameters used to generate the six baseline virtual subjects used in this study. The original values used in Charlton et al. [12] are also shown for comparison, along with a justification for using the new values. Parameters shown as an array of six values correspond to the values used from the 25-year-old to the 75-year-old baseline subjects.

Parameters	New values	Original values	Justification
Heart rate (bpm)	[72.1 74.0 74.9 74.9 73.9 72.0]	[72.9 76.8 77.7 77.3 76.5 74.4]	Male subjects from Fig. 1 in Yashin et al. [54]
Stroke volume (ml)	[71.9 67.9 63.8 59.7 55.6 51.5]	[66.3 63.8 61.3 58.8 56.2 53.7]	Values increased to compensate for the decrease in cardiac output [Le et al. [28]] produced by the lower new heart rate values
Head-and-neck luminal radii	See Supplementary Material Tables S2 to S7	See Supplementary Material Tables S2 to S7	Adjusted to reflect corresponding age-varying *in vivo* measurements more accurately, as described in Section 2.1
Compliances of vascular beds	See Supplementary Material Tables S2 to S7	See Supplementary Material Tables S2 to S7	Adjusted based on Kondiboyina et al. [27] for all terminal vessels
Peripheral vascular resistances of the efferent head arteries	See Supplementary Material Tables S2 to S7	See Supplementary Material Tables S2 to S7	Varied with age (Fig. 2C) to better describe *in vivo* mean flows measured in the common carotid and vertebral arteries, while maintaining the same total peripheral resistance for the entire head vessels
Total peripheral vascular resistance (mmHg min/l)	[10.75; 11.68; 12.93; 13.83; 14.81; 16.14]	[11.52; 11.97; 12.97; 13.61; 14.14; 14.97]	Adjusted to maintain the same mean arterial blood pressure for each age group as in Charlton et al. [12], due to the changes in cardiac output introduced by the new heart rate and stroke volume values
Pulse wave velocities	$k_1 = 4.5 \times 10^6$ g·s^{-2}·cm^{-1} $k_2 = -9$ cm^{-1} $k_3 = 374{,}910 - 2{,}741 \times \text{age} + 247 \times \text{age}^2$ g·s^{-2}·cm^{-1}	$k_1 = 3 \times 10^6$ g·s^{-2}·cm^{-1} $k_2 = -13.5$ cm^{-1} $k_3 = 430{,}118 - 1{,}871.3 \times \text{age} + 244.11 \times \text{age}^2$ g·s^{-2}·cm^{-1}	k_1 and k_2 were adjusted to provide a more accurate description of the carotid artery waveform. Subsequently, k_3 values were calculated for each subject as described in the Appendix of Charlton et al. [12]. Here mean ± SD values of k_3 are provided for the entire population

complete CoW model. To simulate PWs that are representative of healthy adults within each age decade between 25 and 75 years, the model input parameters of the corresponding baseline subjects were adjusted using the approach described in [12] with the modifications outlined in Table 1 and additional details provided next.

The diameters of all head-and-neck arterial segments were adjusted based on age (see Fig. 2A,B and Supplementary Tables S2–S7), following studies by [35,7,10]. The diameters of the carotid sinus and ophthalmic arteries were adjusted according to the criteria used for the internal carotid artery (ICA), while the branches of the external carotid artery (ECA) were adjusted to the criteria used for the ECA.

Particle swarm optimisation (PSO) was used to optimise the proximal resistance (R_1) of the three-element Windkessel model at the outlet of each terminal 1-D model artery in the head (Fig. 1A illustrates the Windkessel model), while keeping the total resistance constant. Subsequently, distal resistance (R_2) values were adjusted. The PSO iterative algorithm aimed to match the age-dependent *in vivo* indices shown in Fig. 3 and Supplementary Material Fig. S2, and to minimise differences between *in silico* and *in vivo* common carotid artery (CCA) and middle cerebral artery (MCA) flow velocity waves (Fig. 4). The PSO approach has been successfully used in several biomechanics applications [47,48,2]. In Charlton et al.'s [12] model, R_1 was set equal to the characteristic impedance (Z_c) of the corresponding terminal 1-D model artery. However, in this study, R_1 was allowed to vary from Z_c by a factor within 0.5 to 1.5, describing downstream vessels forming bifurcations that are not fully well-matched for forward-travelling pulse waves [5]. Further details on the PSO algorithm are provided in Supplementary Material Appendix B and Fig. S1. The modified Windkessel parameters for the six baseline subjects are presented in Supplementary Material Tables S2 to S7. Due to the lack of relevant clinical data, arterial diameters and Windkessel parameters at the outflow boundary conditions were assumed to remain unchanged, irrespective of the CoW variation.

The study used Charlton et al.'s [12] methodology to create a database of 30,618 subjects from the six modified baseline subjects described above. From each baseline subject, $3^6 = 729$ subjects with a complete CoW were generated at each age decade from 25 to 75 years, by varying six cardiovascular parameters that strongly influence PWs [12] in combination with each other by ± 1 SD from their age-specific mean values, namely heart rate, stroke volume, left ventricular ejection time, large artery diameter, pulse wave velocity, and peripheral vascular resistance. This resulted in $6 \times 729 = 4{,}374$ subjects with a complete CoW in the database. The same methodology was repeated for each of the incomplete CoW topologies depicted in Fig. 1B, resulting in an additional $6 \times 4{,}374 = 26{,}244$ subjects and a total of 30,618 subjects.

A quantitative evaluation of the improvements in arterial flow waveforms achieved with our new model was conducted by calculating root-mean-square errors (RMSEs) for all the simulated waveforms shown in Fig. 4 with an *in vivo* counterpart. The following formula was used,

$$RMSE = \sqrt{\frac{\sum_i^N (\bar{x}_i - \hat{x}_i)^2}{N}}, \qquad \bar{x} = \frac{x - \min(x)}{\max(x) - \min(x)}, \qquad \hat{x} = \frac{\check{x} - \min(x)}{\max(x) - \min(x)} \tag{1}$$

where x is the *in vivo* waveform, $\bar{x}$ is the normalised *in vivo* waveform, $\check{x}$ is the *in silico* waveform, $\hat{x}_i$ is the normalised *in silico* waveform, and N is the total number of data points in each waveform.

2.2. Machine learning classifiers

Two artificial neural network (ANN) architectures, namely convolutional neural network (CNN) and multilayer perceptron (MLP), were used to classify different combinations of blood velocity PWs measured in the common carotid and vertebral arteries, with or without brachial blood pressure or velocity PWs, into one of the seven CoW variations depicted in Fig. 1B. A schematic of both architectures is shown in Fig. 5, while Table 2 summarises their main characteristics. Both architectures were built using the open-source library TensorFlow 2.12 [1], Keras Application programming interface [64], and the Scikit-learn Python package [40].

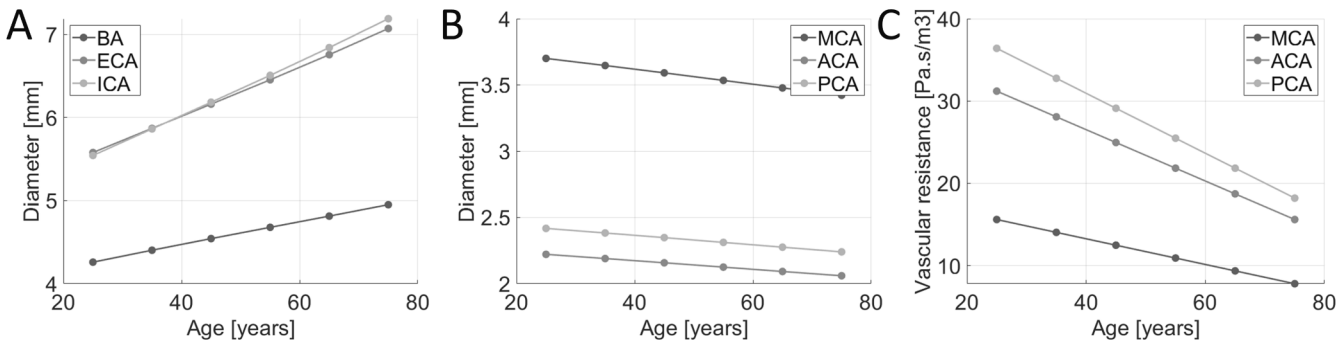

Fig. 2. Variation with age in the luminal radii of the neck (A) and cerebral (B) arteries, and in total cerebral vascular resistance beds (i.e., $R_1 + R_2$ in Fig. 1A) (C). BA: basilar artery; ECA: external carotid artery; ICA: internal carotid artery; MCA: middle cerebral artery; ACA: anterior cerebral artery; PCA: posterior cerebral artery.

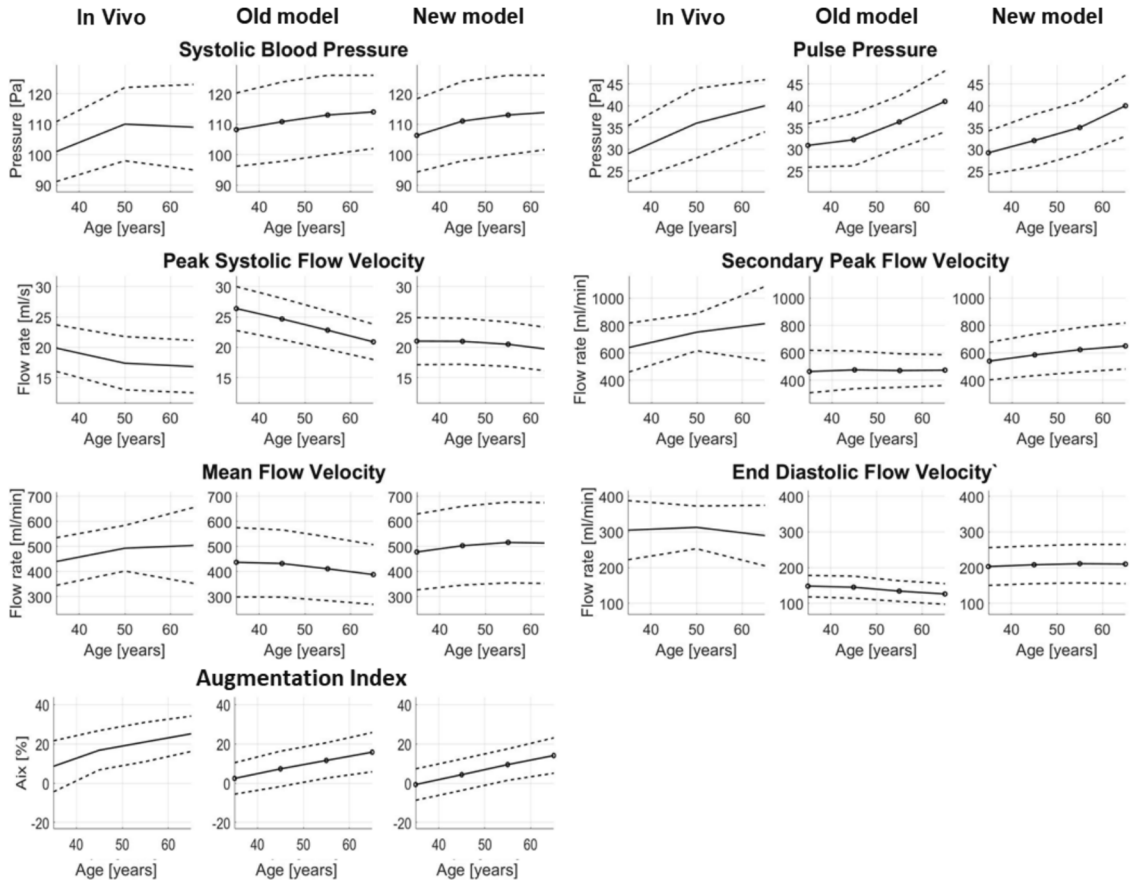

Fig. 3. Comparison between simulated and *in vivo* age-varying haemodynamic characteristics of the right common carotid artery. Each set of three plots shows *in vivo* data (on the left) and simulated data using the old model (in the middle) and the new model (on the right). Solid lines indicate mean values, and dashed lines indicate ± 1SD. In vivo data are from Hirata et al. [20] and Vlachopoulos et al. [53], with sample sizes ranging from 56 to 998 subjects.

The CNN architecture uses convolutional layers to extract features from PWs through compounded nonlinear mapping, generating more features compared to classical techniques such as Fourier transforms [63]. Since CNN models require waveforms of equal length as input, we used one-second waveforms with 275 time-steps, covering an entire cardiac cycle and part of the next. This approach enables the system to learn from variations in heart rate (associated with age), eliminating the need to use age as an input.

For the MLP method, single-cycle waveforms were parametrised using the following nine features of flow velocity (illustrated in Fig. 5C): peak systolic flow velocity (V_s), end-diastolic flow velocity (V_{ed}), peak flow velocity of the secondary rise (V_{sr}), incisura velocity between systole and diastole (V_i), mean flow velocity (V_m), time to peak systolic flow velocity (T_s), time to peak flow velocity of the secondary rise (T_{sr}), time to incisura between systole and diastole (T_i), and duration of the cardiac cycle (T_{cc}) [41]. For blood pressure, the following five features were used: systolic pressure, diastolic pressure, mean pressure, time to systolic pressure, and duration of the cardiac cycle.

Five additional ML models were tested to benchmark the performance of the ANN architectures. These models, using the same input features as MLP, include gradient boosting (GB) [15,14], random forest (RF) [30,8], logistic regression (LR) [50,24], support vector machine (SVM) [56], and naive Bayes (NB) [43]. These techniques were selected for their robustness, as they exhibit minimal sensitivity to hyperparameters and are less susceptible to overfitting compared to more complex ML models. Furthermore, they represent a range of

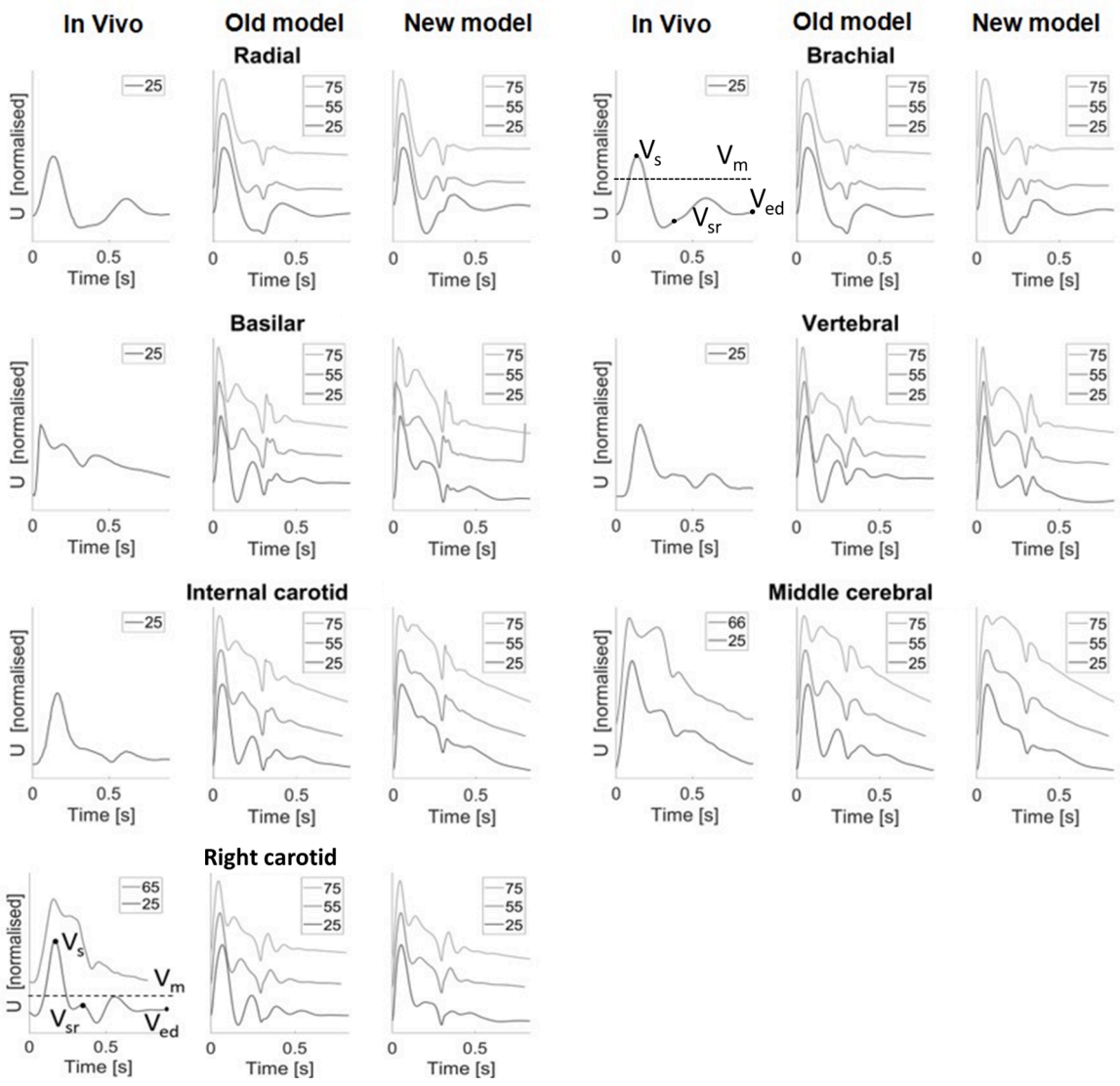

Fig. 4. Comparison between simulated and *in vivo* flow velocity pulse waveforms (PWs). Each set of three plots shows *in vivo* PWs (on the left), and simulated PWs using the old model by Charlton et al. [12] (in the middle) and our new model (on the right). PWs are shown for different ages in each plot (*in vivo* only if data was available), offset and normalized. Legends indicate ages. The *in vivo* brachial and carotid artery plots illustrate the following fiducial points: peak systolic velocity (V_s), end-diastolic velocity (V_{ed}), peak velocity of the secondary rise (V_{sr}), and mean velocity (V_m). In vivo data is from Kondiboyina et al. (2022a), Reymond et al. [42] and Hirata et al. [20], with sample sizes ranging from 7 to 56 subjects.

probabilistic (GB, NB and LR) and non-probabilistic (RF and SVM) approaches, ensuring diverse modelling strategies [22].

2.2.1. *Training and testing*

The *in silico* PW database, comprising 30,618 subjects, was randomly split into training (80 %) and testing (20 %) sets. For training, a multi-class classification strategy was applied, where each of the seven CoW variations was represented by one of the output neurons. The softmax activation function applied to the output layer ensures that each neuron outputs a real number between 0 and 1, representing the probability of the corresponding CoW variation being present. The sum of the output values across all neurons equals 1, and the neuron with the highest output value indicates the most likely detected variation. The trained ML models were then evaluated on the testing set to assess their ability to detect different CoW topologies. A total of 45 different input configurations were tested for the ML classifiers, as detailed in Supplementary Material Table S8.

The hyperparameter optimisation followed a three-step strategy across all models. First, a grid search systematically explored a range of hyperparameter settings for each model. Second, each set of hyperparameters was evaluated using k-fold cross-validation (k = 10) to ensure robust performance estimates, independent of specific data partitions. Third, the same performance metric was used for optimisation, maintaining the same number of iterations and folds during cross-validation. Additional details on the hyperparameter optimisation process are provided in Supplementary Material Appendix C.

To examine the impact of noise on PW signals across all ML architectures, artificial Gaussian white noise was added to the input PWs at several noise-to-signal ratios: 5 %, 10 %, 15 %, and 20 % [16]. The noise was introduced to the raw PW signals before extracting the input wave features. All ML models were trained and tested with and without noise, using the same 80 %-20 % training–testing split (24,494 and 6,124 subjects, respectively). Training was conducted with noise levels randomly varying between 0 % to 20 %, while testing was performed on datasets with fixed noise levels of 0 %, 5 %, 10 %, 15 %, and 20 %, each containing 6,124 subjects.

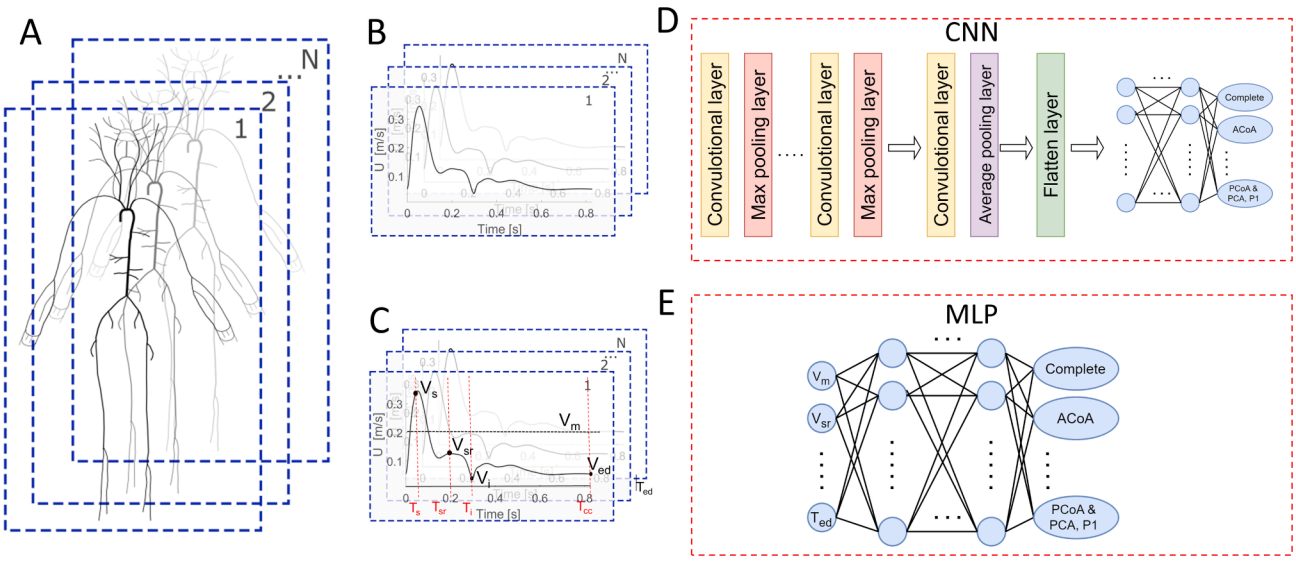

Fig. 5. Schematic of the (D) convolutional neural network (CNN) and (E) multilayer perceptron (MLP) architectures used for classifying circle of Willis topology. (A) Simulated blood velocity (*U*) pulse waves in N = 30,618 virtual subjects were used as input data for training both the CNN and MLP. (B) The entire waveform was used as input to the CNN. (C) Nine features calculated from the *U* pulse wave were used as input to the MLP.

Table 2
Characteristics of the convolutional neural network (CNN) and multilayer perception (MLP) architectures for classifying circle of Willis topology.

Parameters	CNN	MLP
Number of hidden layers	5	10
Number of neurons	10	10
Number of convolutional layers	5	–
Kernel	3	–
Type of input	Waveform	Waveform features (N = 9)
Number of outputs	7 CoW anatomies	7 CoW anatomies
Optimizer	Adam	Adam
Batch size	128	128
Loss function	Binary classification	Binary classification
Number of epochs	1,000	1,000
Activation functions	Relu (hidden layer) – Softmax (output layer)	Relu (hidden layer) – Softmax (output layer)

2.2.2. Performance metrics

The F1-score was used in a one-vs-rest manner to evaluate the quality of the multiclass classification results. This metric, commonly employed for assessing binary classification models that classify outputs as either 'positive' or 'negative,' was used to assess the models' ability to distinguish the class of interest from the remaining classes when creating individual binary classifiers for each class in the multiclass problem. For instance, when calculating the F1-score for the complete CoW, all incomplete CoW topologies were grouped into a single class, while complete CoW formed the other class. The results are reported as the mean F1-score across all CoW topologies.

The F1-score is calculated by taking the harmonic mean of the model's precision and recall, with both precision and recall being equally weighted in the F1-score [46,25]. Precision represents the proportion of true positive cases (TP) among those labelled as positive by the model, calculated as the number of TP divided by the total number of false positives (FP) plus TP. Recall, also known as sensitivity, indicates the proportion of positive instances among the total number of positive examples and is calculated as the number of TP divided by the sum of false negatives (FN) and TP.

$$F1-score = \frac{2Precision^{*}Recall}{Precision + Recall} \tag{2}$$

$$Precision = \frac{TP}{TP + FP} \tag{3}$$

$$Recall = \frac{TP}{TP + FN} \tag{4}$$

Additionally, the receiver operating characteristic (ROC) curve and the area under the ROC curve (AUC) [9] were also used to evaluate the ability of the ML models to accurately classify CoW topology for each class in a one-vs-rest manner. The ROC curve is widely used to demonstrate the balance between recall and specificity (the ability of the model to correctly identify true negative cases) at various classification thresholds. Curves that approach the top-left corner indicate superior performance. The AUC represents the probability that the model will rank a positive case higher than a negative case. It ranges between 0 and 1, where 0 indicates that the model made all predictions incorrectly, and 1 indicates that the model made all predictions correctly.

2.2.3. SHAP (SHapley Additive exPlanations)

To interpret the predictions of our ANN architectures, we used SHapley Additive exPlanations (SHAP) [33]. SHAP is a method from cooperative game theory that assigns an importance value to each feature for a given prediction. In ML, SHAP values quantify the contribution of each feature to a model's prediction, centred around zero, with their sum explaining the deviation of the given prediction from the mean prediction. The magnitude and range of SHAP values depend on the specific dataset, features, and the model itself. The SHAP value ($\varnothing_i$) for a feature i is calculated as

$$\varnothing_i = \sum_{S \subseteq N \setminus \{i\}} \frac{|S|!(|N| - |S| - 1)!}{|N|!} [E[f(x)|x_s \cup \{i\}] - E[f(x)|x_s]] \tag{5}$$

where $f(x)$ is the model's prediction function, N is the set of all features, S is a subset of features from N, x_s is a subset of the input feature vector x that includes only the features specified by S, $E[f(x)|x_s]$ is the expected value of the model's prediction given only the features in subset S are known, with other features marginalised, and $E[f(x)|x_s \cup \{i\}]$ is the expected value of the model's prediction given both the features in S and feature i are known. The mean SHAP value for a feature i across all

instances in a dataset of M instances is

$$mean[|\varnothing_i|]_i = \frac{1}{M}\sum_{j=1}^{M}\left|\varnothing_i^j\right| \quad (6)$$

where $\varnothing_i^j$ is the SHAP value of feature i for the j-th instance in the dataset. This average helps understand the overall impact of a feature across all predictions.

To interpret the CoW topology predictions generated by our CNN and MLP models, we used the SHAP library's 'DeepExplainer' function, which is well-suited for analysing ANNs. This explainer was initialised with each model and a subset of the training data comprising 2,000 subjects. This setup enabled the explainer to learn how each feature influenced the CoW topology predictions. We used a separate test subset containing 300 subjects. We analysed the input PW data containing blood flow velocity waveforms from the left and right common carotid and vertebral arteries, without added noise, to study the effect of these waveforms individually. For MLP, the nine derived features from each waveform illustrated in Fig. 5C were considered. For CNN, the flow velocity magnitude at each time step in the waveform was analysed. We then calculated mean SHAP values across 10 different testing subsets. These mean SHAP values revealed how much each feature contributed to the difference between the actual prediction and the average prediction.

3. Results

3.1. New dataset characteristics

The PWs obtained with the new model exhibit two main improvements compared to those obtained with the old model by Charlton et al. [12]. Firstly, the timing and magnitude of the second flow peak in the basilar, vertebral, internal carotid, middle cerebral, and common carotid arteries at 25 years, and of the middle cerebral artery at 65 years, align more closely with the respective *in vivo* values (Fig. 4), resulting in considerably smaller root mean square errors between *in vivo* PWs and the corresponding simulated PWs using the new model (Supplementary Material Table S10). Secondly, both the trends and magnitudes of several PW indices calculated in the common carotid artery better approximate the corresponding *in vivo* indices with age (Fig. 3). These indices include all four flow velocity features depicted in Fig. 4 (bottom).

The morphology of PWs in non-head-and-neck arteries showed minimal differences between both models. For example, the flow velocity PWs in the radial and brachial arteries shown in Fig. 4, the pressure PW in the aorta, common carotid, radial, and digital arteries, the finger and ear photoplethysmography PW (Supplementary Material Fig. S4), as well as the PW indices calculated from the aortic and brachial pressures (Supplementary Material Fig. S2), all exhibited small disparities between the two models. However, it is worth noting that some improvements were observed specifically at the finger site: the new model better captured the diastolic peak of both the PPG and pressure PWs in the finger for a young subject (Supplementary Material Fig. S4).

None of the six CoW topologies studied caused significant alterations in the PW morphology of non-head-and-neck arteries, including the brachial artery (Fig. 6). However, notable PW variations were observed in the vertebral and basilar arteries, particularly in CoW variations that involve a missing artery in the posterior circulation. Relatively smaller PW variations were observed in the common carotid and middle cerebral arteries. These results were consistent across different age groups (Fig. 6 shows results for the 25-year-old baseline subject and Supplementary Material Figs. S5 and S6 for the 55- and 75-year-old baseline subjects, respectively).

3.2. Machine learning classification

Fig. 7 compares the mean F1-score achieved for all seven ML models trained using various combinations of PW input data. These scores are tabulated in Supplementary Material Table S8. Overall, the ANN architectures produced higher F1-scores compared to the other five models, with the CNN model often outperforming the MLP model. Among the other five models, random forest, gradient boosting, and support vector machine performed similarly for all input data combinations, while logistic regression and naive Bayes had the lowest scores. All models achieved higher F1-scores ($\leq$0.96) when including two or more input waves, compared to single wave inputs ($\leq$0.76). This trend is

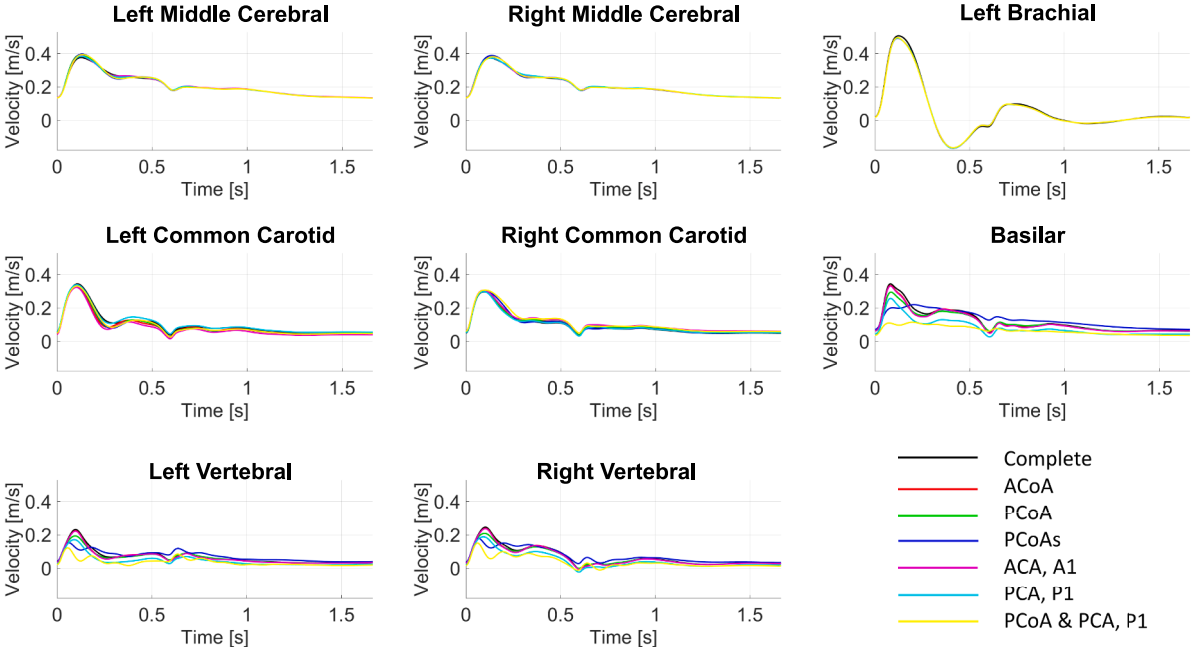

Fig. 6. Comparison of simulated velocity pulse waveforms (PWs) in neck-and-head and left brachial arteries for all studied circle of Willis topologies, for the 25-year-old baseline subject. Each plot shows seven PWs at the same arterial site, one for each topology.

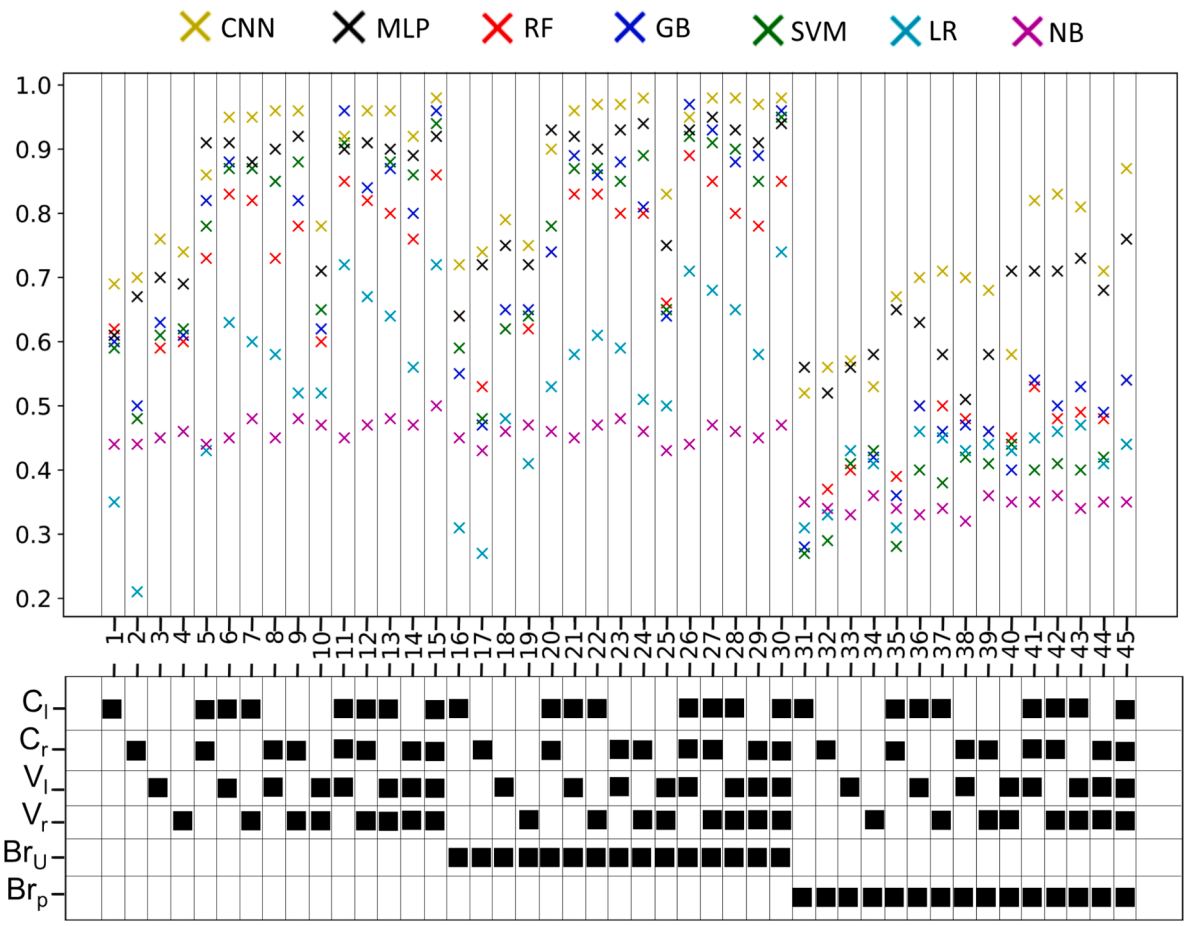

Fig. 7. Comparison of mean F1-scores among seven machine learning models for forty-five different combinations of input pulse waves. C_l: left common carotid blood flow velocity, C_r: right common carotid blood flow velocity, V_l: left vertebral blood flow velocity, V_r: right vertebral blood flow velocity, Br_u: left brachial blood flow velocity, Br_p: left brachial blood pressure.

also highlighted in the F1-score boxplot for the CNN model (Supplementary Material Fig. S7), which compares different numbers of input waves.

Combining a carotid and a vertebral input flow velocity wave yielded a higher mean F1-score ($\leq$0.96) compared to using either carotid or vertebral flow velocity waves ($\leq$0.91). Adding the left brachial artery flow velocity pulse wave to all combinations of carotid and vertebral velocity waves resulted in minor improvements in the F1-scores. Lastly, including the left brachial blood pressure along with all combinations of carotid and vertebral velocity waves worsened F1-scores.

Fig. 8 (top) shows the confusion matrices for the CNN and MLP models trained and tested with flow velocity waveforms from the right common carotid and vertebral arteries (the combination of two input pulse waves that yielded the highest F1-scores for both models). The CNN model had a higher true prediction rate than the MLP model (mean: 98 % vs. 95 %). The anatomical variations with the lowest prediction rates were the cases where the segment ACA A1 was missing for CNN and where the ACoA was missing for MLP. Supplementary Material Fig. S8 shows the confusion matrices for the five additional ML models examined, demonstrating reasonable performances by random forest, gradient boosting, and support vector machine (prediction rates > 85 %), while logistic regression and naive Bayes were less able to classify CoW anatomical variations (prediction rates < 69 %). CNN consistently outperformed MLP across all age groups (mean F1-scores > 0.97 vs. > 0.90, Table 3), with both models' performance declining with age. The ROC curves displayed excellent sensitivity and specificity for all CoW topologies (Fig. 8, bottom), with AUC values over 0.99 for CNN and 0.93 for MLP (Table 4). Both models effectively differentiated between among classes, although the missing ACoA topology had the lowest AUC values.

The SHAP analysis identified the mean velocity (V_m) and the peak systolic velocity (V_s) as the primary features influencing the CoW topology predictions of the MLP model (Fig. 9). Time features had a lesser impact compared to magnitude features, with the duration of the cardiac cycle (T_{cc}) being the most influential among them. The incisura velocity between systole and diastole (V_i) and the peak flow velocity of the secondary rise (V_{sr}) were also ranked among the top 20 features. For the CNN model, the velocity values up to the time of V_s were the most influential features for both the carotid and vertebral arteries. Additionally, the velocity values around and particularly after the time of V_i were important for the carotid arteries (Fig. 10).

3.3. *Effect of simulated measurement noise*

As noise levels increased, F1-scores for all models and training cases decreased (Fig. 11). However, training with noise led to higher F1-scores at any given noise level. The CNN model outperformed the MLP model, except for the highest noise level of 20 % (0.75 vs. 0.79). Among the other five models, the support vector machine maintained high F1-scores (0.75 at 20 % noise) when trained with noise (Supplementary Material Figure S9). Logistic regression and naive Bayes were less sensitive to noise and training case, but had lower F1-scores overall, below 0.6 and 0.4 respectively.

Supplementary Material Figure S10 shows the impact of noise on the confusion matrices obtained for all seven models. Training with noise improved the number of true predictions for all models except naive

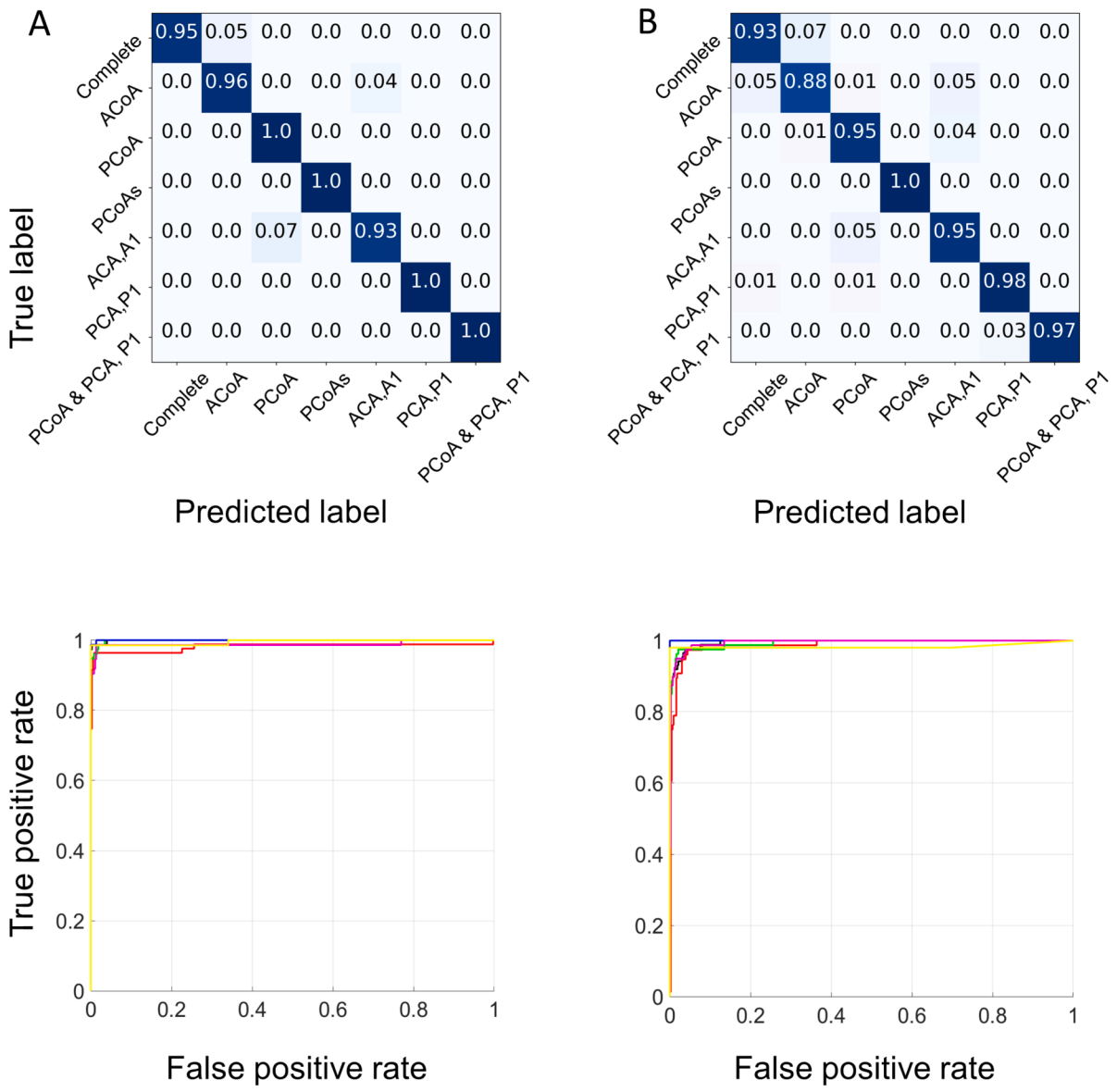

Fig. 8. Performance of the CNN (A) and MLP (B) models when trained and tested using the flow velocity waveforms in the right common carotid and vertebral arteries as input data. Confusion matrix (top) and ROC curves (bottom) for all the circle of Willis topologies. The colour code for the ROC curves corresponds to the one used in Fig. 6.

Table 3
Mean F1-scores for each age group produced by the convolutional neural network (CNN) and multilayer perception (MLP) models, with the flow velocity waveforms in the right common carotid and vertebral arteries as input data.

Age	CNN	MLP
25	0.987	0.921
35	0.984	0.923
45	0.986	0.922
55	0.975	0.914
65	0.967	0.906
75	0.971	0.902

Bayes. Notably, models exhibited the highest true prediction rates when both posterior communication arteries were absent, except for MLP. Among all models, MLP yielded the highest true predictions rate.

For CNN and MLP models, AUC values for detecting CoW anatomical variations decreased with increasing noise levels (Table 4). Training with noise resulted in higher AUC values, with MLP outperforming CNN for noise levels above 10 %. Both models achieved higher AUC values for anatomical variation with missing posterior arteries and the lowest AUC values for variations with missing anterior arteries, particularly the ACoA.

4. Discussion

This is the first study to demonstrate the feasibility of predicting the CoW topology in healthy individuals using artificial neural network (ANN) architectures analysing carotid and vertebral artery flow velocity waveforms, which can be noninvasively acquired through Doppler ultrasound. Our proposed ML analysis of neck artery velocity waveforms offers a potential noninvasive and cost-effective alternative to angiography methods, such as computed tomography and magnetic resonance, which involve ionising radiation or contrast agents. Our findings show that ANN architectures considerably improve predictive capabilities compared to non-ANN models, except for support vector machine, which maintained comparable predictive power when trained with

Table 4
Area under the curve (AUC) values produced by the convolutional neural network (CNN) and multilayer perception (MLP) models when classifying the seven circle of Willis topologies studied using the flow velocity waveforms in the right common carotid and vertebral arteries as input data. Both models were trained with noise levels randomly varied from 0% to 20%, and then tested against datasets with fixed noise levels of 0%, 5%, 10%, 15%, and 20%.

CNN without noise	**Complete**	**ACoA**	**PCoA**	**PCoAs**	**ACA, A1**	**PCA, P1**	**PCoA & PCA, P1**
0 % noise level	0.999	0.989	0.998	0.999	0.997	0.999	0.998
5 % noise level	0.987	0.966	0.987	0.989	0.983	0.987	0.989
10 % noise level	0.944	0.885	0.973	0.979	0.962	0.979	0.972
15 % noise level	0.879	0.789	0.949	0.969	0.907	0.969	0.965
20 % noise level	0.805	0.758	0.929	0.958	0.874	0.963	0.959
CNN with noise	**Complete**	**ACoA**	**PCoA**	**PCoAs**	**ACA, A1**	**PCA, P1**	**PCoA & PCA, P1**
0 % noise level	0.998	0.982	0.999	0.999	0.991	1	0.998
5 % noise level	0.987	0.961	0.989	0.988	0.970	0.989	0.985
10 % noise level	0.965	0.923	0.975	0.978	0.918	0.975	0.979
15 % noise level	0.941	0.859	0.962	0.967	0.837	0.962	0.969
20 % noise level	0.921	0.847	0.914	0.948	0.844	0.958	0.951
MLP without noise	**Complete**	**ACoA**	**PCoA**	**PCoAs**	**ACA, A1**	**PCA, P1**	**PCoA & PCA, P1**
0 % noise level	0.968	0.935	0.960	0.995	0.969	0.995	0.998
5 % noise level	0.920	0.830	0.934	0.985	0.921	0.985	0.984
10 % noise level	0.840	0.692	0.857	0.975	0.881	0.974	0.971
15 % noise level	0.778	0.641	0.784	0.962	0.836	0.959	0.962
20 % noise level	0.739	0.615	0.736	0.946	0.793	0.942	0.943
MLP with noise	**Complete**	**ACoA**	**PCoA**	**PCoAs**	**ACA, A1**	**PCA, P1**	**PCoA & PCA, P1**
0 % noise level	0.972	0.948	0.979	0.995	0.977	0.991	0.995
5 % noise level	0.956	0.927	0.971	0.986	0.963	0.982	0.978
10 % noise level	0.945	0.902	0.957	0.977	0.945	0.981	0.971
15 % noise level	0.930	0.879	0.946	0.966	0.921	0.965	0.962
20 % noise level	0.925	0.862	0.937	0.956	0.908	0.960	0.958

noise-added PWs. Additionally, all ML models demonstrated superior performance in identifying CoW topologies with missing posterior communication arteries compared to those with missing anterior arteries.

The main challenge with the two ANN models we studied (i.e., CNN and MLP) was optimising their architectures and hyperparameters. The hyperparameter optimisation strategy used in this study ensured a fair comparison of models by minimising biases and fully optimising each model within our dataset. Once optimised, CNN, with its ability to automatically detect features from PWs, proved more effective in detecting subtle topology-induced changes, achieving the highest F1-scores. This model demonstrated a promising ability to classify conditions based on pulse wave profiles more effectively than the nine scalar features initially selected. This suggests that CNN may leverage complex, nonlinear features inherent in waveform data that are not captured by the traditional scalar metrics used in the MLP model. However, both MLP and CNN models have significant room for further improvement as the potential architectures that could be explored are vast. In contrast, non-ANN models consistently showed lower predictive performance across all input combinations of PW signals. These results are in line with previous research applying these non-ANN models for detecting vascular conditions like stenosis and aneurysms based on PWs [24,23].

Our findings indicate that distinguishing between different PW morphologies poses challenges for naive Bayes (NB) and logistic regression (LR) methods. In contrast, random forest (RF), gradient boosting (GB), and support vector machine (SVM) demonstrated greater potential for effectively classifying haemodynamic data, particularly with appropriate parameter optimisation. This suggests that the intricate interplay between carotid and vertebral flow velocities and the CoW topology cannot be adequately captured by linear models like NB and LR. However, nonlinear models such as RF, GB, and SVM can capture the complex patterns and relationships within the haemodynamic data, leading to more accurate classification outcomes.

When simulating clinical conditions, we introduced random noise to all input data to test the models' robustness across various noise scenarios, ensuring models were not excessively tuned to any specific noise level. This included accounting for higher noise levels in the vertebral artery, due to interference from surrounding vertebrae, compared to the carotid artery. Our results indicate that the models maintained resilience to varying noise levels. CNN architectures exhibited improved predictive capabilities with clean waveforms, capturing intricate patterns and relationships without relying heavily on specific wave features. However, with noisy waveforms, MLP and SVM models performed better, suggesting that feature-based data inputs are less susceptible to noise, especially when the model architecture is complex enough to accurately represent the underlying relationships. SVMs, in particular, prioritise the most relevant support vectors, acting as an implicit feature selection mechanism, allowing them to outperform other methods in noisy data scenarios by focusing on the most informative data points.

The SHAP analysis revealed that the mean velocity (V_m) and peak systolic velocity (V_s) were the main features influencing CoW topology predictions in the MLP model. Other velocity features, such as the incisura velocity between systole and diastole (V_i) and the peak flow velocity of the secondary rise (V_{sr}), generally exhibited smaller changes compared to V_m and V_s. This made them mathematically less distinguishable due to their smaller variation. Time features had less impact compared to velocity features, indicating that they are less affected by the CoW topology. This is because time features are mainly related to heart rate variability and pulse wave speeds, which did not significantly change with variations in CoW topology. For the CNN model, the SHAP analysis identified the most influential features as the velocity values up to the time of V_s and those around and particularly after the time of V_i as. This highlights the importance of V_s, similar to the MLP model. The CNN's ability to analyse velocities before V_s and around V_i, which were not included as inputs in the MLP, may explain why the CNN outperformed the MLP.

All ML models performed better in detecting CoW topologies with missing posterior arteries than those with other missing arteries. The absence of specific posterior arteries significantly impacted vertebral artery blood flow velocity, aiding model detection. However, distinguishing between a complete CoW and one lacking only the ACoA was more challenging due to the minimal blood flow through the ACoA under healthy conditions, resulting in limited haemodynamic changes in the neck arteries. In contrast, the absence of an anterior cerebral artery considerably affected common carotid artery blood flow, making this anatomical variation easier to detect than a missing ACoA.

Age had a small effect on prediction accuracy, with only a 2 % difference observed between older and younger samples. This variation may be attributed to the sharper waveform peaks found in older subjects compared to the smoother waveforms of younger subjects. ML

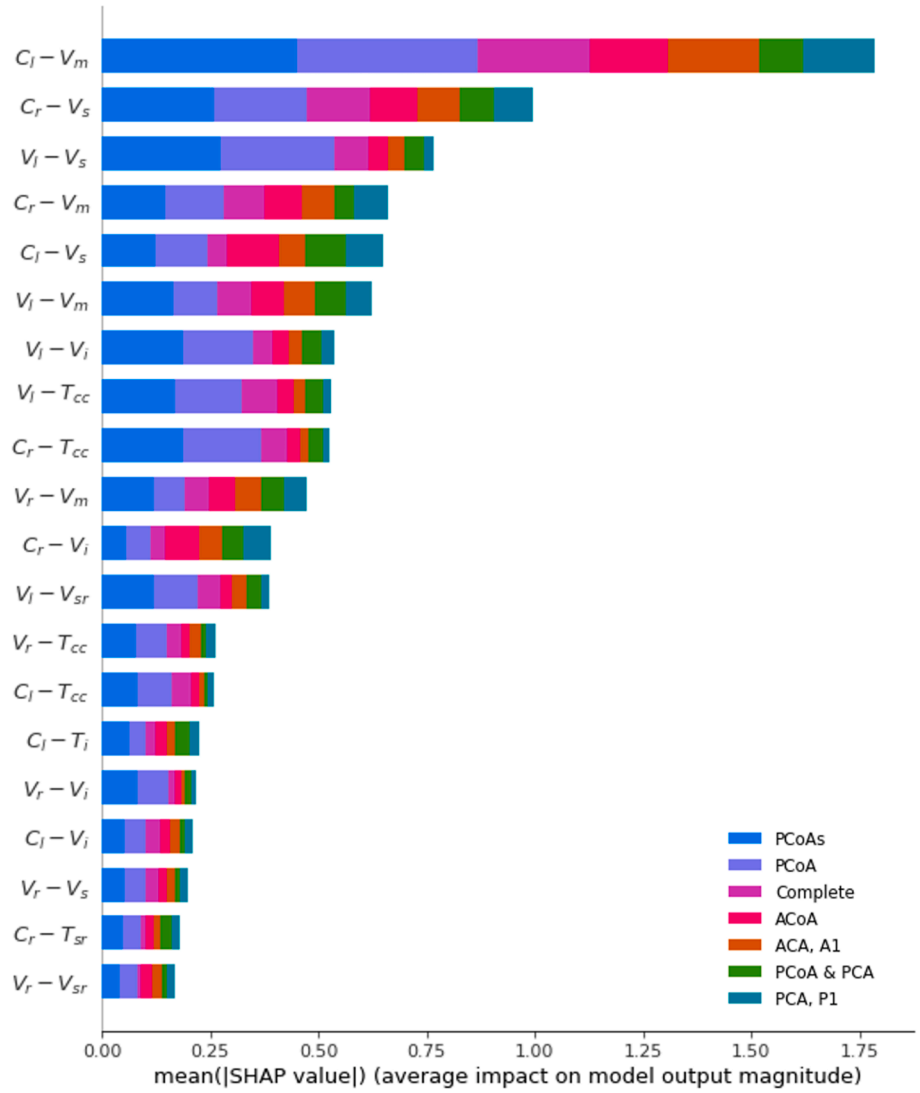

Fig. 9. Top 20 mean SHAP values for the multilayer perceptron (MLP) model across the seven circle of Willis topologies (as indicated by the legend colours), using the input flow velocity waveforms from the left (C_l) and right (C_r) common carotid arteries, and the left (V_l) and right (V_r) vertebral arteries. Mean values calculated across 10 different training and test samples, for nine derived features from these waveforms: peak systolic velocity (V_s), end-diastolic velocity (V_{ed}), peak velocity of the secondary rise (V_{sr}), incisura velocity between systole and diastole (V_i), mean velocity (V_m), time to peak systolic velocity (T_s), time to peak velocity of the secondary rise (T_{sr}), time to incisura velocity between systole and diastole (T_i), and duration of the cardiac cycle (T_{cc}).

algorithms often struggle with sharp waveforms [26], which could reduce prediction accuracy in older populations.

This study has several limitations. First, our method was tested solely on *in silico* data. Although the *in silico* PW signals showed realistic age-related changes in the aorta and peripheral arteries, including the cerebral circulation, further research is needed to assess the generalisability of the findings to real patients across all ages. Second, the dataset consists only of healthy adult samples, so the findings may not generalise to cohorts with pathophysiological conditions. The variation in cardiovascular parameters when simulating PWs was limited to normal values (within ± 1 SD of age-specific mean values) and, hence, our analysis does not consider outlying physiology. Moreover, instead of varying the properties of each artery individually, we changed the properties (diameter and pulse wave velocity) of the entire arterial network together within ± 1 SD. This approach captures overall differences in the scale and stiffness of the arterial network (relative to age), but it does not account for local variations in arterial characteristics, such as the size ratio between individual arteries. Third, while we accounted for instrumental noise, we did not consider the impact of physiological noise, such as motion artefacts, commonly encountered in physiological signal measurement. Finally, we assumed fixed flow rate distributions in the efferent CoW arteries to focus on structural differences and their impact on cerebral perfusion without the added complexity of variable flow rates due to cerebral flow autoregulation mechanisms. This assumption does not capture the individual variability in flow rate distributions seen in real-world scenarios, which may affect the accuracy of our results.

4.1. Perspectives

While CTA and MRA are effective in detecting CoW topology, they are time-consuming, costly, and involve ionising radiation or contrast agents. Our *in silico* study offers valuable insights for future clinical investigations using Doppler ultrasound as an alternative method that does not involve ionising radiation or contrast agents, making it safer for repeated use. Additionally, Doppler ultrasound is generally faster, less costly, and can be performed with portable equipment, increasing its practicality and accessibility. Our findings suggest that carotid and vertebral flow velocity waveforms alone provide sufficient information for ML-based classification of CoW topology, eliminating the need for

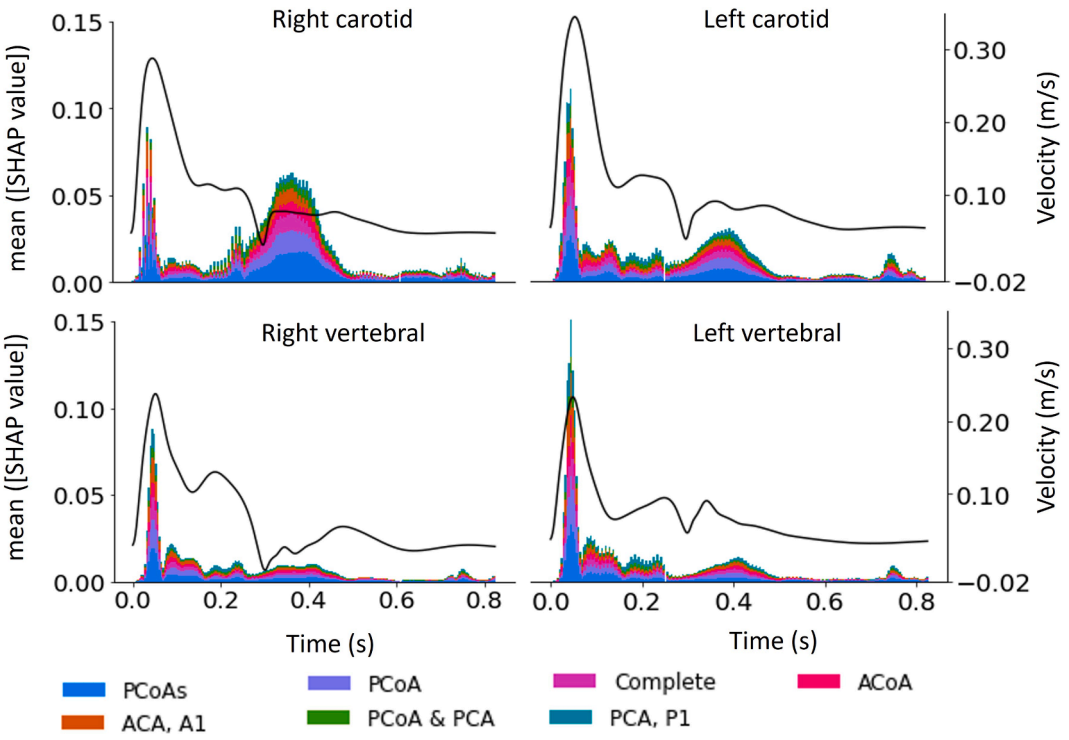

Fig. 10. Mean SHAP values for the convolutional neural network (CNN) model across the seven circle of Willis topologies (as indicated by the legend colours), using the input flow velocity waveforms from the left and right common carotid arteries, and the left and right vertebral arteries. Mean SHAP (left y-axes) values with time across 10 different training and test samples for the right common carotid (top left), left common carotid artery (top right), right vertebral artery (bottom left), and left vertebral artery (bottom right). Flow velocity (right y-axes, solid lines) with time for the 25-year-old baseline subject.

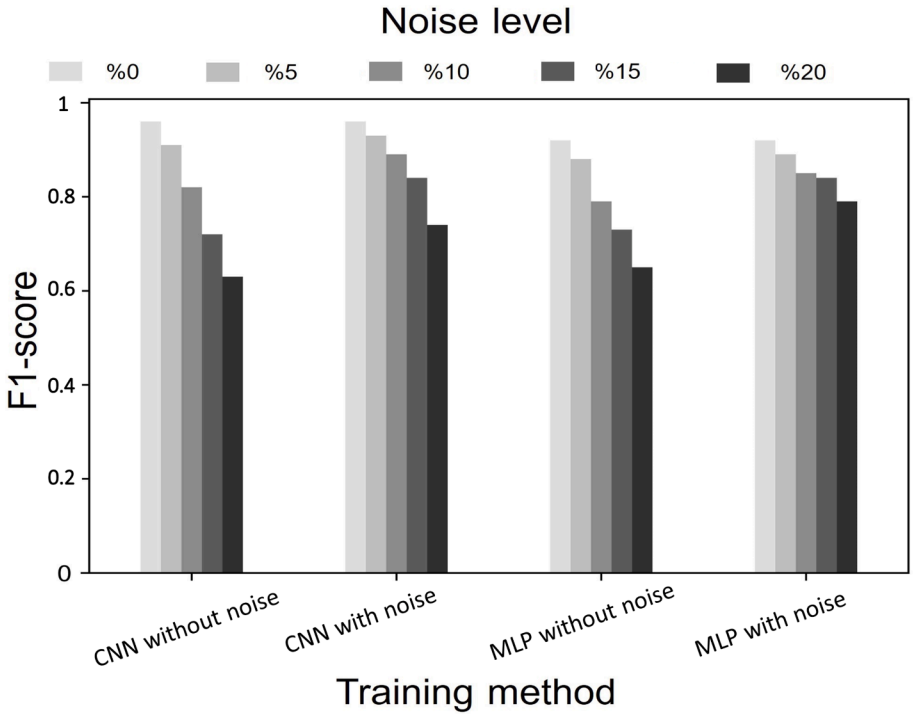

Fig. 11. Impact of noise on CNN and MLP performance. Mean F1-scores for CNN and MLP models trained with right common carotid and vertebral artery flow velocity waveforms, across noise levels of 0, 5, 10, 15, and 20%.

additional PW measurements from other arterial sites (e.g., brachial flows or pressures). Therefore, future clinical studies on assessing cerebrovascular risk could focus solely on acquiring neck flow velocity waveforms using a single Doppler ultrasound device.

This article is accompanied by resources to support the development and testing of other ML methods involving PWs in the larger arteries of the systemic circulation. These resources, available on Zenodo [https://zenodo.org/records/12519322], include the complete new dataset

comprising PWs from 30,618 virtual subjects, MATLAB functions for post-processing this dataset, and the code for training and testing all ML models using the open-source library TensorFlow 2.12, the Keras application programming interface, and the Scikit-learn Python package.

5. Conclusion

This *in silico* study has demonstrated that the circle of Willis topology can be accurately classified using machine learning models, specifically multi-layer perceptron (MLP) and convolutional neural network (CNN) architectures. The MLP, with features extracted from one vertebral and one common carotid blood velocity pulse waveform, performed well with noise that mimics real *in vivo* measurement errors. The CNN, processing the entire waveform, excelled with noise-free data across all ages. SHapley Additive exPlanations (SHAP) analysis revealed mean and peak systolic velocities as the primary features influencing predictions. Although further evaluation on *in vivo* data involving both healthy and diseased subjects is necessary, our approach holds promise for assessing disease risk and aiding preoperative decision-making in cerebral circulation.

CRediT authorship contribution statement

Ahmet Sen: Writing – original draft, Visualization, Software, Methodology, Investigation, Formal analysis, Data curation, Conceptualization. **Miquel Aguirre:** Writing – review & editing, Supervision, Resources, Project administration, Funding acquisition. **Peter H Charlton:** Writing – review & editing, Resources. **Laurent Navarro:** Writing – review & editing, Supervision, Project administration. **Stéphane Avril:** Writing – review & editing, Supervision, Resources, Funding acquisition. **Jordi Alastruey:** Writing – review & editing, Writing – original draft, Visualization, Validation, Supervision, Software, Resources, Project administration, Methodology, Investigation, Funding acquisition, Conceptualization.

Declaration of competing interest

The authors declare that they have no known competing financial interests or personal relationships that could have appeared to influence the work reported in this paper.

Data availability

This article is accompanied by resources to support the development and testing of other ML methods involving PWs in the systemic circulation's larger arteries (published in Zenodo)

Acknowledgements

This work represents independent research partially supported by the British Heart Foundation Grants PG/15/104/31913 and FS/20/20/34626. The authors acknowledge support from the National Institute for Health and Care Research (NIHR) HealthTech Research Centre (HRC) in Cardiovascular and Respiratory Medicine at Guy's and St Thomas' NHS Foundation Trust and King's College London. The views expressed are those of the authors and not necessarily those of the BHF, NHS, the NIHR or the Department of Health and Social Care.

Appendix A. Supplementary data

Supplementary data to this article can be found online at https://doi.org/10.1016/j.bspc.2024.106999.

References

[1] Abadi, M., Agarwal, A., Barham, P., Brevdo, E., Chen, Z., Citro, C., ... Zheng, X. (2015). *TensorFlow: Large-scale machine learning on heterogeneous systems.* Retrieved from https://www.tensorflow.org/ (Software available from tensorflow.org).
[2] Y. Aboelkassem, D. Savic, Particle swarm optimizer for arterial blood flow models, Comput. Methods Programs Biomed. 201 (2021) 105933.
[3] J. Alastruey, K. Parker, J. Peiró, S.M. Byrd, S. Sherwin, Modelling the circle of Willis to assess the effects of anatomical variations and occlusions on cerebral flows, J. Biomech. 40 (8) (2007) 1794–1805.
[4] J. Alastruey, S.M. Moore, K.H. Parker, T. David, J. Peiró, S. Sherwin, Reduced modelling of blood flow in the cerebral circulation: Coupling 1-D, 0-D and cerebral auto-regulation models, Int. J. Numer. Meth. Fluids 56 (2008) 1061–1067.
[5] J. Alastruey, K.H. Parker, J. Peiró, S.J. Sherwin, Lumped parameter outflow models for 1-D blood flow simulations: effect on pulse waves and parameter estimation, Comm. Comput. Phys. 4 (2) (2008) 317–336.
[6] J. Alastruey, P.H. Charlton, V. Bikia, B. Paliakaitė, B. Hametner, R.M. Bruno, B. E. Westerhof, Arterial pulse wave modelling and analysis for vascular age studies: a review from VascAgeNet, American Journal of Physiology-Heart and Circulatory Physiology 325 (1) (2023) H1–H29.
[7] Arsalidou, M., Skuratov, N., Khalezov, E., Bernstein, A., Burnaev, E., & Sharaev, M. (2022). Effects of age, gender, and hemisphere on cerebrovascular hemodynamics in children and young adults: Developmental scores and machine learning classifiers. *Plos One, 17*(2), e0263106.
[8] L. Breiman, Random forests, Mach. Learn. 45 (2001) 5–32.
[9] C.D. Brown, H.T. Davis, Receiver operating characteristics curves and related decision measures: A tutorial, Chemom. Intel. Lab. Syst. 80 (1) (2006) 24–38.
[10] A.H. Brohi, K.J.J. Borges, N. Hassan, M. Ali, S.N.N. Shah, G.H. Yar, Variation in Calibre of Arteries of Circle of Willis with Age: An MRA Based Study, Annals of Abbasi Shaheed Hospital and Karachi Medical & Dental College 23 (4) (2018) 184–190.
[11] N.K. Chakshu, I. Sazonov, P. Nithiarasu, Towards enabling a cardiovascular digital twin for human systemic circulation using inverse analysis, Biomech. Model. Mechanobiol. 20 (2) (2021) 449–465.
[12] P.H. Charlton, J. Mariscal Harana, S. Vennin, Y. Li, P. Chowienczyk, J. Alastruey, Modeling arterial pulse waves in healthy aging: a database for in silico evaluation of hemodynamics and pulse wave indexes, American Journal of Physiology-Heart and Circulatory Physiology 317 (5) (2019) H1062–H1085.
[13] A.J. Einstein, Medical imaging: the radiation issue, Nat. Rev. Cardiol. 6 (6) (2009) 436–438.
[14] J. Elith, J.R. Leathwick, T. Hastie, A working guide to boosted regression trees, J. Anim. Ecol. 77 (4) (2008) 802–813.
[15] J.H. Friedman, Greedy function approximation: a gradient boosting machine, Ann. Stat. (2001) 1189–1232.
[16] N.R. Gaddum, J. Alastruey, P. Beerbaum, P. Chowienczyk, T. Schaeffter, A technical assessment of pulse wave velocity algorithms applied to non-invasive arterial waveforms, Ann. Biomed. Eng. 41 (2013) 2617–2629.
[17] A. Gupta, H. Baradaran, A. Schweitzer, H. Kamel, A. Pandya, D. Delgado, P. Sanelli, Oxygen extraction fraction and stroke risk in patients with carotid stenosis or occlusion: a systematic review and meta-analysis, Am. J. Neuroradiol. 35 (2) (2014) 250–255.
[18] A. Gupta, J.L. Chazen, M. Hartman, D. Delgado, N. Anumula, H. Shao, et al., Cerebrovascular reserve and stroke risk in patients with carotid stenosis or occlusion: a systematic review and meta-analysis, Stroke 43 (11) (2012) 2884–2891.
[19] L.B. Hindenes, A.K. Haberg, L.H. Johnsen, E.B. Mathiesen, D. Robben, T. R. Vangberg, Variations in the Circle of Willis in a large population sample using 3D TOF angiography: The Tromsø Study, PLoS One 15 (11) (2020) e0241373.
[20] K. Hirata, T. Yaginuma, M.F. O'Rourke, M. Kawakami, Age-related changes in carotid artery flow and pressure pulses: possible implications for cerebral microvascular disease, Stroke 37 (10) (2006) 2552–2556.
[21] W. Jin, P. Chowienczyk, J. Alastruey, Estimating pulse wave velocity from the radial pressure wave using machine learning algorithms, PLoS One 16 (6) (2021) e0245026.
[22] G. Jones, J. Parr, P. Nithiarasu, S. Pant, Machine learning for detection of stenoses and aneurysms: application in a physiologically realistic virtual patient database, Biomech. Model. Mechanobiol. 20 (6) (2021) 2097–2146.
[23] G. Jones, J. Parr, P. Nithiarasu, S. Pant, A physiologically realistic virtual patient database for the study of arterial haemodynamics, International Journal for Numerical Methods in Biomedical Engineering 37 (10) (2021) e3497.
[24] G. Jones, J. Parr, P. Nithiarasu, S. Pant, A proof of concept study for machine learning application to stenosis detection, Med. Biol. Eng. Compu. 59 (10) (2021) 2085–2114.
[25] G. Jones, J. Parr, P. Nithiarasu, S. Pant, A proof of concept study for machine learning application to stenosis detection, Med. Biol. Eng. Compu. 59 (2021), https://doi.org/10.1007/s11517-021-02424-9.
[26] G. Kissas, Y. Yang, E. Hwuang, W.R. Witschey, J.A. Detre, P. Perdikaris, Machine learning in cardiovascular flows modeling: Predicting arterial blood pressure from non-invasive 4D flow MRI data using physics-informed neural networks, Comput. Methods Appl. Mech. Eng. 358 (2020) 112623.
[27] A. Kondiboyina, H.A. Harrington, J.J. Smolich, M.M. Cheung, J.P. Mynard, Optimized design of an arterial network model reproduces characteristic central and peripheral haemodynamic waveform features of young adults, J. Physiol. 600 (16) (2022) 3725–3747.

[28] T.T. Le, R.S. Tan, M. De Deyn, E.P.C. Goh, Y. Han, B.R. Leong, C.W.L. Chin, Cardiovascular magnetic resonance reference ranges for the heart and aorta in Chinese at 3T, J. Cardiovasc. Magn. Reson. 18 (2016) 1–13.
[29] J. Li, L. Zheng, W.J. Yang, C.Y. Sze-To, T.W.H. Leung, X.Y. Chen, Plaque wall distribution pattern of the atherosclerotic Middle Cerebral Artery Associates with the Circle of Willis completeness, Front. Neurol. 11 (2021) 599459.
[30] A. Liaw M. Wiener Classification and regression by random forest R News 2 3 2002 18–22 (ISSN: 1609–3631).
[31] E.C. Lin, Radiation risk from medical imaging, In *Mayo Clinic Proceedings* (vol. 85 (2010) 1142–1146.
[32] Lippert, H. & Pabst, R. (1985). *Arterial Variations in Man: Classification and Frequency*. Springer.
[33] S.M. Lundberg, S.-I. Lee, A unified approach to interpreting model predictions, Adv. Neural Inf. Proces. Syst. 30 (2017) 4765–4774.
[35] S. Mujagic, M. Moranjkic, N. Mesanovic, S. Osmanovic, The inner diameter of arteries of the circle of Willis regarding gender and age on magnetic resonance angiography, Acta Medica Saliniana 42 (2) (2013) 6.
[38] T. Ouyoung, W.L. Weng, T.Y. Hu, C.C. Lee, L.W. Wu, H. Hsiu, Machine-Learning Classification of Pulse Waveform Quality, Sensors 22 (22) (2022) 8607.
[39] T. Padayachee, F. Kirkham, R. Lewis, J. Gillard, M. Hutchinson, R. Gosling, Transcranial measurement of blood velocities in the basal cerebral arteries using pulsed Doppler ultrasound: a method of assessing the Circle of Willis, Ultrasound Med. Biol. 12 (1) (1986) 5–14.
[40] F. Pedregosa, G. Varoquaux, A. Gramfort, V. Michel, B. Thirion, O. Grisel, et al., Scikitlearn: Machine learning in python, The Journal of Machine Learning Research 12 (2011) 2825–2830.
[41] A. Rahman Rasyada, A. Azhim, Flow velocity in common carotid artery, IntechOpen (2018), https://doi.org/10.5772/intechopen.80712.
[42] P. Reymond, F. Merenda, F. Perren, D. Rufenacht, N. Stergiopulos, Validation of a one-dimensional model of the systemic arterial tree, American Journal of Physiology-Heart and Circulatory Physiology 297 (1) (2009) H208–H222.
[43] I. Rish, J. Hellerstein, J. Thathachar, An analysis of data characteristics that affect naive Bayes performance, IBM TJ Watson Research Center 30 (2001) 1–8.
[44] Rosner, J., Reddy, V., & Lui, F. (2018). Neuroanatomy, Circle of Willis.
[45] D.J. Ryan, S. Byrne, R. Dunne, M. Harmon, J. Harbison, White matter disease and an incomplete circle of Willis, Int. J. Stroke 10 (4) (2015) 547–552.
[46] Y. Sasaki, 01), The truth of the F-measure, Teach Tutor Mater, 2007.
[47] Schutte, J. F., Koh, B.-I., Reinbolt, J. A., Haftka, R. T., George, A. D., & Fregly, B. J. (2005). Evaluation of a particle swarm algorithm for biomechanical optimization. J Biomech Eng. 2005 Jun;127(3):465-74. doi: 10.1115/1.1894388.
[48] A. Sen, H. Follet, E. Sornay-Rendu, Y. Rémond, D. George, Prediction of osteoporotic degradation of tibia human bone at trabecular scale, J. Mech. Behav. Biomed. Mater. 105650 (2023).
[49] A. Sen, L. Navarro, S. Avril, M. Aguirre, A data-driven computational methodology towards a pre-hospital Acute Ischaemic Stroke screening tool using haemodynamics waveforms, Comput. Methods Programs Biomed. 244 (2024) 107982.
[50] S. Sperandei, Understanding logistic regression analysis, Biochemia Medica 24 (1) (2014) 12–18.
[51] H. Tanaka, N. Fujita, T. Enoki, K. Matsumoto, Y. Watanabe, K. Murase, H. Nakamura, Relationship between variations in the circle of Willis and flow rates in internal carotid and basilar arteries determined by means of magnetic resonance imaging with semiautomated lumen segmentation: reference data from 125 healthy volunteers, Am. J. Neuroradiol. 27 (8) (2006) 1770–1775.
[52] A. Varga, G. Di Leo, P.V. Banga, C. Csobay-Novák, M. Kolossváry, P. Maurovich-Horvat, K. Hüttl, Multidetector CT angiography of the circle of Willis: association of its variants with carotid artery disease and brain ischemia, Eur. Radiol. 29 (1) (2019) 46–56.
[53] C. Vlachopoulos, M. O'Rourke, W.W. Nichols, McDonald's Blood Flow in Arteries: Theoretical, CRC Press, Experimental and Clinical Principles, 2011.
[54] A.I. Yashin, I.V. Akushevich, K.G. Arbeev, L. Akushevich, S.V. Ukraintseva, A. Kulminski, Insights on aging and exceptional longevity from longitudinal data: novel findings from the Framingham Heart Study, Age 28 (2006) 363–374.
[55] C. Yuhn, M. Oshima, Y. Chen, M. Hayakawa, S. Yamada, Uncertainty quantification in cerebral circulation simulations focusing on the collateral flow: Surrogate model approach with machine learning, PLoS Comput. Biol. 18 (7) (2022) e1009996.
[56] L. Wang, Support Vector Machines: Theory and Applications, Vol. 177, Springer Science & Business Media, 2005.
[57] S. Wang, R. Ono, D. Wu, K. Aoki, H. Kato, T. Iwahana, H. Liu, Pulse wave-based evaluation of the blood-supply capability of patients with heart failure via machine learning, Biomed. Eng. Online 23 (1) (2024) 7.
[58] T. Wang, W. Jin, F. Liang, J. Alastruey, Machine learning-based pulse wave analysis for early detection of abdominal aortic aneurysms using in silico pulse waves, Symmetry 13 (5) (2021) 804.
[59] T. Wang, F. Liang, L. Li, W. Zhang, G. Wang, J. Wang, X. Qi, A computational model-based study on the exchangeability of hepatic venous pressure gradients measured in multiple hepatic veins, Med. Eng. Phys. 84 (2020) 28–35.
[60] W. Wang, Q. Wang, M. Qiu, A. Pan, G. Yang, A review of the circle of Willis: investigative methods, anatomical variations and correlated ischemic brain diseases, Sci Insigt 33 (2) (2020) 159–166.
[61] M. Willemet, P. Chowienczyk, J. Alastruey, A database of virtual healthy subjects to assess the accuracy of foot-to-foot pulse wave velocities for estimation of aortic stiffness, American Journal of Physiology-Heart and Circulatory Physiology 309 (4) (2015) H663–H675.
[62] P. Wijesinghe, H.W.M. Steinbusch, S.K. Shankar, T.C. Yasha, K.R.D. De Silva, Circle of Willis abnormalities and their clinical importance in ageing brains: A cadaveric anatomical and pathological study, J. Chem. Neuroanat. 106 (2020) 101772.
[63] M. Zubair, J. Kim, C. Yoon, An automated ECG beat classification system using convolutional neural networks, in: In *2016 6th International Conference on IT Convergence and Security (ICITCS)*, 2016, pp. 1–5, https://doi.org/10.1109/ICITCS.2016.7740310.
[64] Chollet, F., & others. (2015). Keras. GitHub. Retrieved from https://github.com/fchollet/keras.

Glossary

ACoA: Anterior communicating artery
ACA: Anterior cerebral artery
ANN: Artificial neural network
AUC: Area under the ROC curve
BA: Basilar artery
bpm: Beats/min
CCA: Common carotid artery
CNN: Convolutional neural network
CoW: Circle of Willis
CTA: Computed tomography angiography
ECA: External carotid artery
GB: Gradient boosting
HR: Heart rate
ICA: Internal carotid artery
LR: Logistic regression
LVET: Left ventricular ejection time
MCA: Middle cerebral artery
ML: Machine learning
MLP: Multilayer perceptron
MRA: Magnetic resonance angiography
NB: Naive Bayes
P: Blood pressure
PCA: Posterior cerebral artery
PCoA: Posterior communicating artery
PPG: Photoplethysmography
PFT: Peak flow time
PSO: Particle swarm optimization
PVC: Peripheral vascular compliance
PVR: Peripheral vascular resistance
PW: Pulse wave
Q: Volume flow rate
RF: Random forest
RFV: Reverse flow volume
ROC: Receiver operating characteristic
SV: Stroke volume
SVM: Support vector machine
VA: Vertebral artery
V_{ed}: End-diastolic flow velocity
V_m: Mean flow velocity
V_s: Peak systolic flow velocity
V_{sr}: Peak flow velocity of the secondary rise
T_{cc}: Duration of the cardiac cycle
T_s: Time to peak systolic flow velocity
T_{sr}: Time to peak flow velocity of the secondary rise
1-D: One-dimensional